PROCEEDINGS, 51st Workshop on Geothermal Reservoir Engineering
Stanford University, Stanford, California, February 9-11, 2026
SGP-TR-230

Coupled Chemical–Mechanical Behavior of Natural Fractures and Its Implications for Proppant Design at Utah FORGE EGS

Ettehadi A.*, Mutume B.

Hydraulic Barrier Material and Geomimicry Laboratory, School of Chemical Engineering, Oklahoma State University, 420 Engineering North, Stillwater, OK, 74078, USA

ali.ettehadi@okstate.edu, bruce.mutume@okstate.edu

Keywords: Utah FORGE; Enhanced Geothermal Systems; Hydrothermal Alteration; Micromechanical Testing; Natural Fractures; Mineralogical Characterization; Proppant Design; Fracture Stability

ABSTRACT

Enhanced Geothermal Systems (EGS) rely on the coupled chemical and mechanical behavior of natural and stimulated fractures to sustain permeability and ensure long-term reservoir stability. At the Utah FORGE site, granitic rocks contain mineral-filled natural fractures whose evolving properties under high-temperature conditions critically influence stimulation performance. This study integrates hydrothermal exposure experiments and micro-scale mechanical characterization to investigate how geochemical alteration modifies the micromechanical behavior of fracture minerals and interfaces, with the objective of deriving fracture-scale constraints relevant to proppant performance in the Utah FORGE reservoir.

A representative granitic core sample extracted from a depth of 9,843 ft was subjected to hydrothermal exposure at 250 °C to simulate EGS reservoir conditions. Nanoindentation testing was performed before and after hydrothermal treatment to quantify changes in hardness and elastic modulus, while X-ray diffraction (XRD) and scanning electron microscopy coupled with energy-dispersive spectroscopy (SEM–EDS) were used to characterize mineralogical and microstructural evolution along fracture surfaces.

Results indicate that hydrothermal interaction produces spatially heterogeneous chemical and mechanical modification of fracture walls, including the development of aluminosilicate alteration coatings, Fe–Al–rich reaction layers, and localized secondary precipitates. These alterations lead to systematic reductions in hardness and elastic modulus in fracture-proximal domains, while relatively unaltered quartz- and feldspar-rich regions retain higher stiffness and brittleness. Such fracture-scale heterogeneity implies non-uniform proppant–fracture contact conditions and evolving load-transfer behavior under EGS operating conditions. Rather than prescribing specific proppant materials, the results provide mineral- and alteration-dependent mechanical constraints that inform proppant design considerations for Utah FORGE, including resistance to embedment in chemically softened fracture zones, tolerance to variable surface compliance, and mechanical robustness against contact with brittle, quartz-dominated domains. By linking fracture geochemistry and micromechanical evolution, this study establishes a mechanistic basis for evaluating proppant performance in crystalline EGS reservoirs.

1. INTRODUCTION

Enhanced Geothermal Systems (EGS) represent a critical pathway for scalable, low-carbon baseload energy production (Azim et al., 2010; Meller et al., 2017; Tester et al., 2007) by enabling heat extraction from low-permeability crystalline reservoirs (Duan et al., 2023; Murphy et al., 1981; Zhang et al., 2012). The long-term performance of EGS reservoirs is governed by the creation, reactivation, and sustained conductivity of fracture networks (Kumawat et al., 2025; Mattson et al., 2016; Pritchett, 2008) subjected to extreme thermal, hydraulic, and chemical conditions (Bächler & Kohl, 2005; Dobson et al., 2021a; Tao et al., 2019). While large-scale stimulation strategies have advanced significantly (Jeanloz & Stone, 2014; Sanyal, 2009; Shan et al., 2024), persistent uncertainty remains regarding the micro-scale mechanisms that control fracture stability, permeability evolution, and mechanical degradation during reservoir operation (Forbes et al., 2019; Miller et al., 2019).

At Utah FORGE, granitic basement rocks host complex natural fracture systems that are commonly sealed or partially infilled by secondary mineral phases formed through hydrothermal alteration (Allard et al., 2003; Jones & Detwiler, 2016; Ledésert et al., 2010). These mineralized fractures exhibit pronounced heterogeneity in composition, microstructure, and mechanical behavior (Ayling et al., 2012; Ye et al., 2020), which directly influences fracture reactivation, shear dilation, and proppant–rock interaction under cyclic thermal and hydraulic loading (Dobson et al., 2021b). Conventional EGS design practices often rely on simplified “hard-rock” assumptions (Willis-Richards et al., 1996), treating crystalline reservoirs as mechanically uniform and chemically inert. Such assumptions neglect the role of mineral-specific mechanical response and chemically induced weakening or strengthening (Callahan et al., 2019; Hueckel et al., 2001; Schuster et al., 2025), potentially leading to suboptimal stimulation outcomes and long-term conductivity loss.

Recent work at Utah FORGE has demonstrated that thermo–hydro–chemical interactions between geothermal fluids, proppants, and reservoir materials drive measurable mineralogical alteration, surface precipitation, and coating degradation under EGS conditions. These studies highlighted strong material- and mineral-dependence in alteration pathways, underscoring that crystalline geothermal reservoirs cannot be treated as chemically or mechanically uniform systems (Ettehadi et al., 2025, 2026; Mutume, Ettehadi, Dhanapala, Palisch, & Radonjic, 2025; Mutume, Ettehadi, Dhanapala, Palisch, Dong, et al., 2025; Mutume, Ettehadi, Radonjic, et al., 2025)

Recent advances in micro- and nano-scale mechanical testing provide a powerful framework for directly quantifying the elastic and plastic behavior of individual mineral phases, fracture fillings, and interfaces (Tyurin et al., 2016; Wu et al., 2024). When combined with controlled hydrothermal exposure experiments, these methods enable direct assessment of how geochemical alteration modifies fracture micromechanics under EGS-relevant conditions (Harpers et al., 2024). Despite this capability, systematic integration of hydrothermal geochemistry, micromechanical characterization, and proppant design remains limited in current EGS research (Frash et al., 2024).

The scope of this work is to investigate the coupled chemical–mechanical evolution of mineralized natural fractures in Utah FORGE granite through hydrothermal treatment and pre- and post-exposure nano-indentation testing, supported by detailed mineralogical and microstructural characterization using XRD and SEM-EDS. The resulting mineral-specific mechanical insights are used to develop a physically grounded proppant design framework aimed at minimizing embedment and crushing while preserving long-term fracture conductivity in crystalline EGS reservoirs.

2. METHODOLOGY

2.1. Sample Selection and Preparation

The material investigated in this study consists of a single intact granite core retrieved from the Utah FORGE Enhanced Geothermal System reservoir. The core was obtained from well 16B-78-32 at a depth of 9843 ft, corresponding to the actively stimulated crystalline reservoir interval. The recovered core preserves natural mineralized fractures and intact grain–boundary interfaces representative of in situ fracture architecture within the EGS reservoir.

Following retrieval, the cylindrical core segment was sectioned using a water-cooled diamond saw to produce a mechanically stable cubic block suitable for hydrothermal exposure and high-resolution surface-based characterization. Initial trimming removed damaged outer surfaces and drilling-induced artifacts, after which orthogonal cuts were performed to define a block geometry while maintaining the orientation and continuity of natural fracture features. The final block dimensions were selected to balance mechanical stability, thermal exposure uniformity, and accessibility for nano-mechanical testing.

One face of the cubic block was designated as the primary characterization surface and was prepared through progressive grinding using silicon carbide papers, followed by fine polishing with diamond suspensions to obtain a flat, smooth surface with minimal preparation-induced damage. This surface preparation protocol ensured compatibility with nano-indentation and scanning electron microscopy while preserving mineral contacts, fracture infill textures, and interface integrity.

Throughout sample preparation, particular care was taken to avoid inducing new microcracks or altering existing fracture geometry. This intact-block approach was deliberately chosen to retain realistic fracture morphology, mineral infill textures, and mechanical boundary conditions relevant to fracture reactivation, embedment behavior in crystalline EGS reservoirs. The prepared granite block was placed in PPL-lined stainless-steel autoclaves and exposed statically at 250 °C for 14 days to simulate reservoir conditions.

2.2. Analytical and Characterization Framework

To resolve mineralogical, structural, and geochemical evolution associated with fluid–rock interaction, an integrated analytical framework was employed combining bulk, microstructural, and fluid-phase characterization techniques. This multi-scale approach enabled direct linkage between mineral transformations, fracture architecture, and fluid chemistry.

Bulk mineralogical composition was quantified using powder X-ray diffraction (XRD). Representative subsamples were finely ground (<62 μm) and analyzed using a Bruker diffractometer equipped with a Cu Kα radiation source operated at 40 kV and 40 mA. Diffraction patterns were collected with a step size of 0.01° and a dwell time of 0.15 s per step, allowing identification of framework silicates, carbonates, and clay minerals, as well as detection of mineralogical changes induced by fluid exposure.

Microstructural and crystallographic characterization was performed using a Focused Ion Beam–Scanning Electron Microscope (FIB–SEM; Scios 2 DualBeam) equipped with energy-dispersive spectroscopy (EDS) and Quasor II electron backscatter diffraction (EBSD). Imaging was conducted primarily in backscattered electron (BSE) mode at 20 keV to enhance mineralogical contrast. EDS and EBSD analyses were used to identify mineral phases, reaction textures, and crystallographic features along grain boundaries and fracture interfaces.

Fluid chemistry following reaction experiments was quantified using inductively coupled plasma mass spectrometry (ICP-MS). Post-reaction fluids were analyzed at Lawrence Berkeley National Laboratory using an Agilent 8900 triple-quadrupole ICP-MS system. Concentrations of 36 major and trace elements were measured under multiple collision and reaction gas modes to minimize spectral interferences. Samples were diluted in 2% HNO_3 prior to analysis, and analytical accuracy was ensured through linear calibration ($R^2 > 0.999$), internal standards (Sc, Ga, Rh, Tm), procedural blanks, and certified reference solutions.

In addition, pH measurements were obtained immediately after cooling samples to room temperature to capture fluid acid–base evolution associated with mineral dissolution, secondary precipitation, and CO_2 buffering. These measurements provided complementary constraints on fluid–rock reaction pathways and geochemical system behavior.

2.3. Integrated Methodology: Pre-Test Microstructural Characterization, Static Hydrothermal Treatment, and Post-Test Mechanical–Microstructural Analysis

The experimental workflow, schematically illustrated in Figure 1, consisted of three sequential and tightly coupled phases designed to capture the chemical–mechanical evolution of mineralized natural fractures under EGS conditions.

2.3.1. Pre-Test Microstructural and Mineralogical Characterization

Prior to hydrothermal exposure, the intact granite block was characterized to establish baseline mineralogical, microstructural, and mechanical properties. Bulk mineralogy was determined using XRD, while polished surfaces were examined using SEM-EDS to identify primary minerals, fracture infill phases, and micro-textures. FIB–SEM equipped with Quasor II electron backscatter diffraction (EBSD) was used on selected regions of interest to resolve crystallographic orientation, grain boundary character, and fracture–matrix interfaces at the micro- to nanoscale. Nano-indentation testing was conducted on representative mineral phases and fracture-adjacent domains to quantify baseline hardness and elastic modulus.

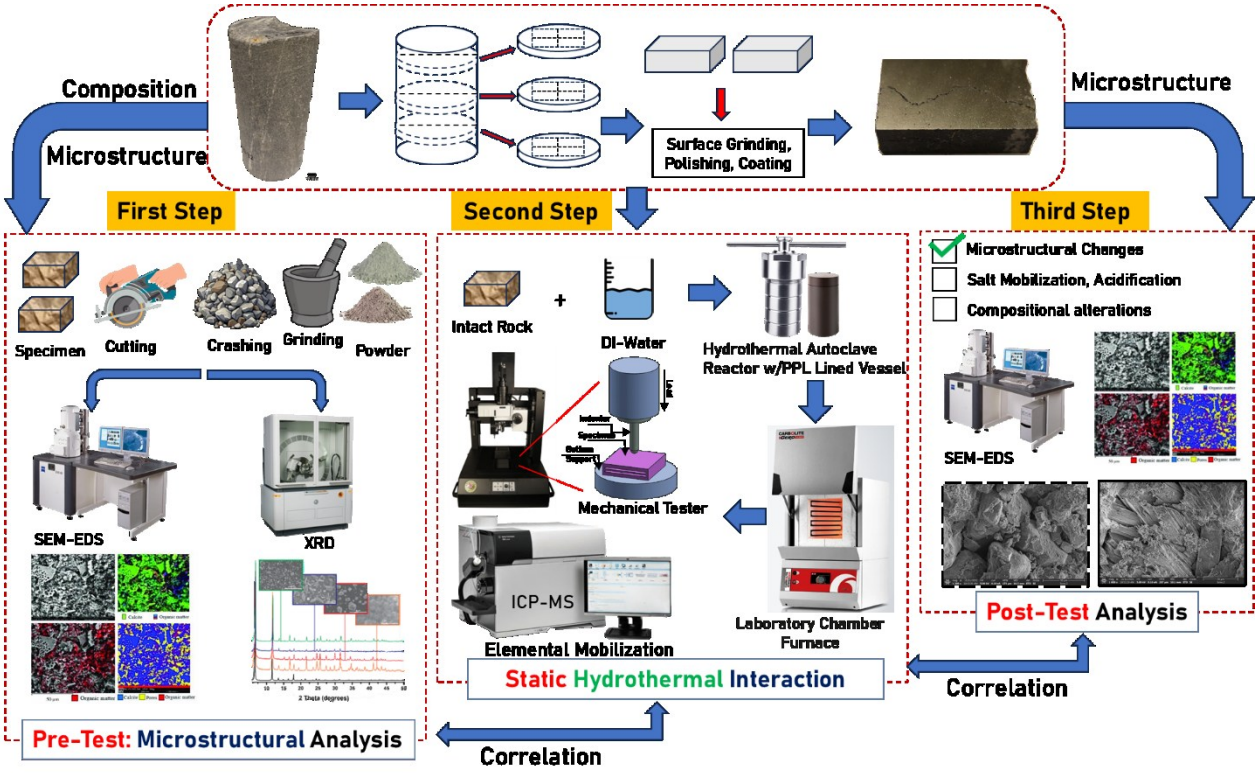

Figure 1. Schematic overview of the experimental methodology, including pre-test microstructural and mineralogical characterization of an intact Utah FORGE granite block, static hydrothermal treatment at reservoir-relevant temperature, and post-test nano-mechanical and microstructural analyses.

2.3.2. Static Hydrothermal Treatment

Following pre-test characterization, the intact granite block was subjected to static hydrothermal treatment at 250 °C under closed-system conditions to simulate geochemical alteration. The sample was placed in a sealed, corrosion-resistant reactor using deionized water as the reacting fluid. This step was designed to promote mineral dissolution, precipitation, and interface modification while preserving the original fracture architecture. After the designated exposure period, the system was cooled gradually to room temperature to minimize thermal shock prior to post-test analysis.

2.3.3. Post-Test Mechanical and Microstructural Analysis

After hydrothermal treatment, the sample was re-examined using SEM-EDS and FIB–SEM/EBSD to identify alteration textures, secondary mineral development, and crystallographic changes along fracture surfaces and grain boundaries. Nano-indentation testing was repeated on closely matched regions analyzed prior to exposure to quantify hydrothermal-induced changes in hardness and elastic modulus. Comparison of pre- and post-treatment datasets enabled direct assessment of how geochemical alteration modifies micromechanical behavior and fracture interface properties under EGS-relevant conditions. This integrated methodology provides a multi-scale framework linking hydrothermal geochemistry, microstructural evolution, and mechanical response, forming the basis for mineral-specific interpretation of fracture stability and proppant–rock interaction in crystalline geothermal reservoirs.

3. RESULTS AND DISCUSSION

3.1. XRD Results and Mineralogical Characterization

X-ray diffraction (XRD) analysis was conducted to quantify the mineralogical composition of the Utah FORGE granite and to place the tested core sample within the broader lithological context of well 16B-78-32. The results are summarized in Figure 2, which presents a three-panel visualization integrating depth-dependent mineralogical trends, sample-specific modal composition, and grouped mineralogical fractions relevant to mechanical interpretation.

Figure 2(a) illustrates the variation in major mineral phases with depth along well 16B-78-32, highlighting the mineralogical continuity and heterogeneity within the crystalline reservoir interval. Feldspar minerals, particularly plagioclase, dominate across the investigated

depth range, while quartz and mafic phases show moderate but persistent contributions. The depth interval corresponding to the tested core sample (~9843 ft) falls within a compositionally representative section of the EGS reservoir, characterized by a feldspar-rich framework with subordinate mafic and accessory minerals. This context confirms that the selected sample is mineralogically consistent with the broader reservoir lithology rather than representing an anomalous local facies.

The modal mineralogical composition of the tested core sample is shown in Figure 2(b) as a donut chart. The assemblage is dominated by framework silicate minerals (~71%), with plagioclase (~61%) constituting the primary load-bearing phase. This high plagioclase content indicates a mechanically stiff crystalline matrix with strong elastic response, while also implying increased susceptibility to brittle fracture under elevated differential stress. Quartz (~6%) contributes additional stiffness and brittleness, particularly along grain boundaries and fracture surfaces, whereas K-feldspar (~4%) complements the feldspathic framework and provides structural rigidity while remaining comparatively less reactive under hydrothermal conditions.

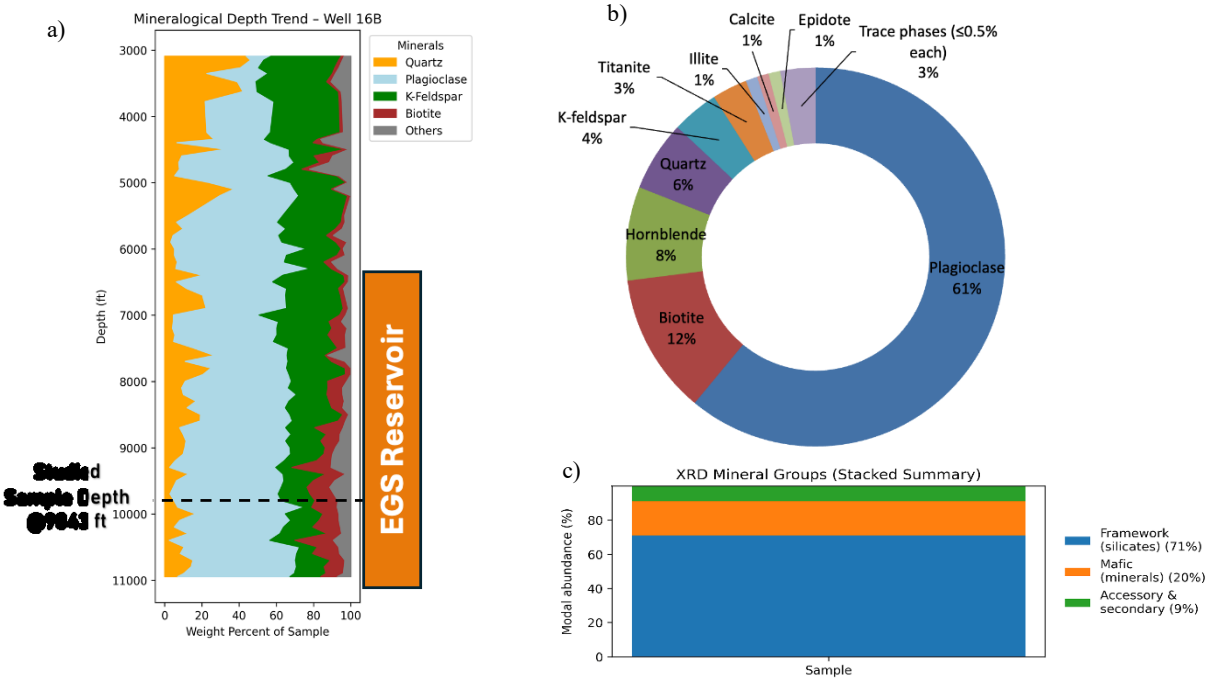

Figure 2. XRD-derived mineralogical characterization of well 16B-78-32 at the Utah FORGE site. (a) **Depth-dependent variation of major mineral phases showing the reservoir context and the sampled interval (~9843 ft).** (b) **Modal mineralogical composition of the analyzed granite core sample from depth of 9843 ft.** (c) **Grouped mineral fractions (framework, mafic, and accessory/secondary) highlighting the mechanically relevant mineral assemblage.**

Mafic minerals account for approximately 20% of the bulk composition, as summarized in Figure 2(c). Biotite (~12%) represents the dominant mafic phase and is mechanically weaker and elastically anisotropic relative to the framework silicates, making it a key control on localized deformation, cleavage-controlled failure, and fracture compliance. Hornblende (~8%), with minor augite present in trace amounts, further contributes to mechanical heterogeneity and may act as preferential sites for stress concentration and hydrothermal alteration within fracture-adjacent domains.

Accessory and alteration-related minerals are present in minor to trace quantities but exert a disproportionate influence on chemical reactivity and fracture evolution. Titanite (~3%) and epidote (~1%) reflect localized hydrothermal alteration and fracture-related mineralization. Carbonate phases, primarily calcite (~1%), introduce mechanically compliant domains that are susceptible to dissolution and chemical softening during hydrothermal exposure. Trace occurrences of illite, chlorite, smectite, siderite, and hematite indicate limited clay and oxide development, suggesting that bulk clay-related weakening is minimal at the sample scale, though locally important along fracture surfaces and alteration halos.

The grouped mineralogical summary shown in Figure 2(c) emphasizes the dominance of a feldspar-rich framework (~71%), with subordinate mafic (~20%) and accessory/secondary (~9%) components. Collectively, these results indicate a mechanically strong yet microscopically heterogeneous crystalline reservoir rock, in which mineral-scale contrasts in stiffness, anisotropy, and chemical stability are expected to govern fracture reactivation behavior, micromechanical variability, and mineral-specific risks of proppant embedment and crushing. This mineralogical framework provides a critical baseline for interpreting the nano-mechanical and hydrothermal response of natural fractures investigated in this study.

3.2. Microstructural and Surface Changes Induced by Hydrothermal Exposure (SEM–BSE Analysis)

Backscattered electron (BSE) imaging was used to evaluate microstructural and surface-level changes induced by hydrothermal exposure at 250 °C. SEM–BSE contrast, which scales with average atomic number, enables identification of mineralogical heterogeneity, fracture

networks, grain boundary evolution, and the development of secondary alteration products. A point-by-point comparison of identical surface locations before and after exposure was conducted to isolate thermally and chemically driven microstructural modifications from pre-existing textural features. Figure 3 shows pre-exposure SEM–BSE images from four selected surface locations (P1–P4), establishing the baseline microstructural state characterized by intact mineral grains, sharp grain boundaries, and inherited fracture features.

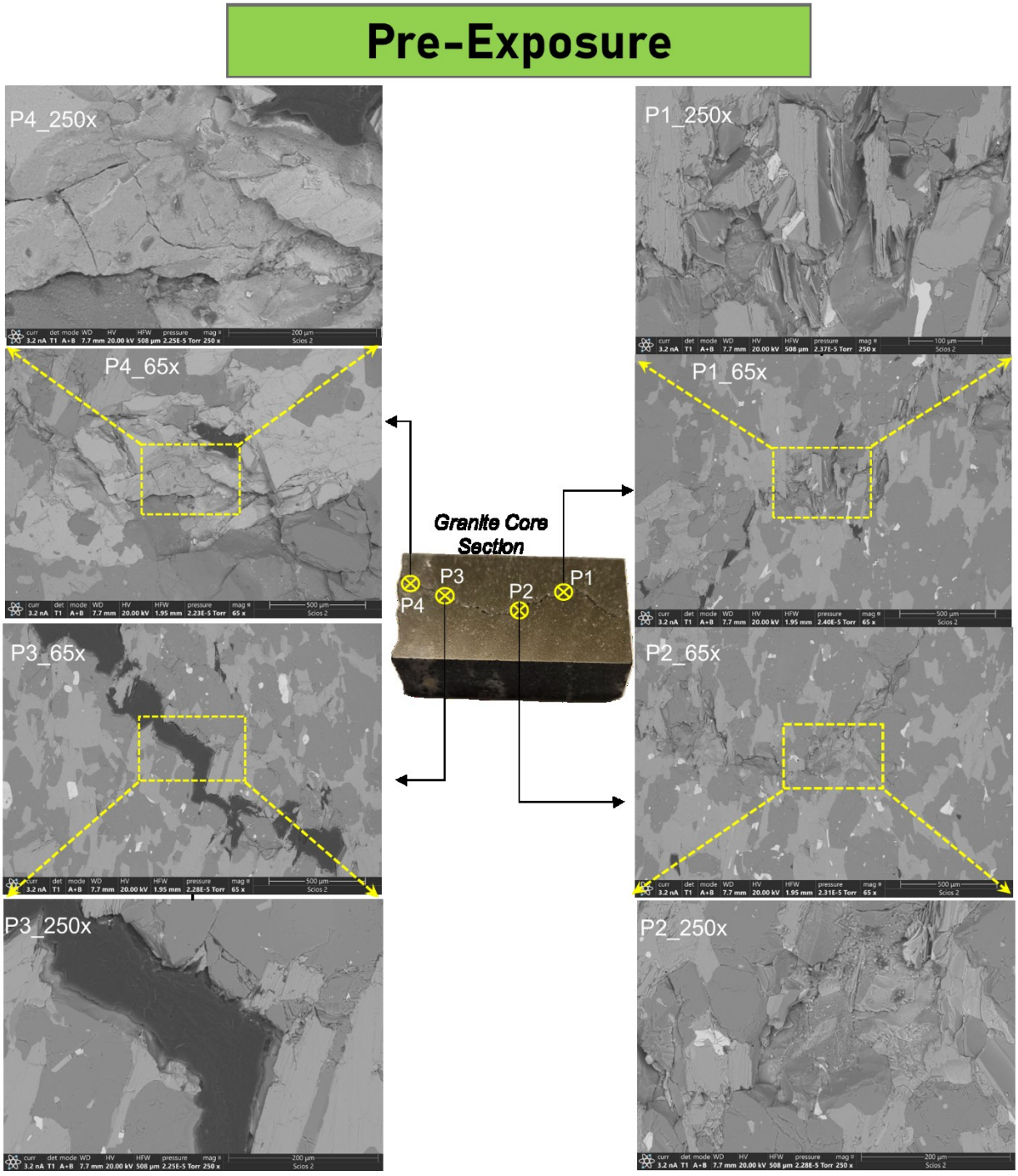

Figure 3. Pre-exposure SEM–BSE microstructural characterization of the granite sample at selected surface locations (P1–P4). Backscattered electron (BSE) images acquired prior to hydrothermal treatment show representative microstructures at four marked surface points on the sample. Low-magnification images (65×) provide spatial context for each analyzed region, while higher-magnification images (250×) highlight grain boundaries, mineral interfaces, and pre-existing fractures. The dashed yellow boxes indicate the regions selected for detailed analysis. The central photograph shows the macroscopic sample with the corresponding analysis points (P1–P4).

Figure 4 presents SEM–BSE images of the same locations following hydrothermal exposure at 250 °C, allowing direct comparison of microstructural evolution under elevated-temperature aqueous conditions. Across all points, hydrothermal exposure results in increased

textural heterogeneity, changes in BSE contrast, and modification of grain boundary and fracture morphology relative to the pre-exposure state. At Points 1 and 2, pre-exposure SEM–BSE images show interlocking grain fabrics with intact grain-to-grain contacts, limited open porosity, and fractures primarily confined to grain boundaries and cleavage-controlled discontinuities, indicating a mechanically coherent microstructural framework prior to hydrothermal exposure. After exposure, both locations exhibit more irregular and locally widened grain boundaries, enhanced fracture connectivity, and diffuse darkening along interfaces. At higher magnification, these regions display mottled BSE contrast consistent with partial dissolution of primary minerals and precipitation of fine-grained secondary alteration material concentrated along structurally weak domains.

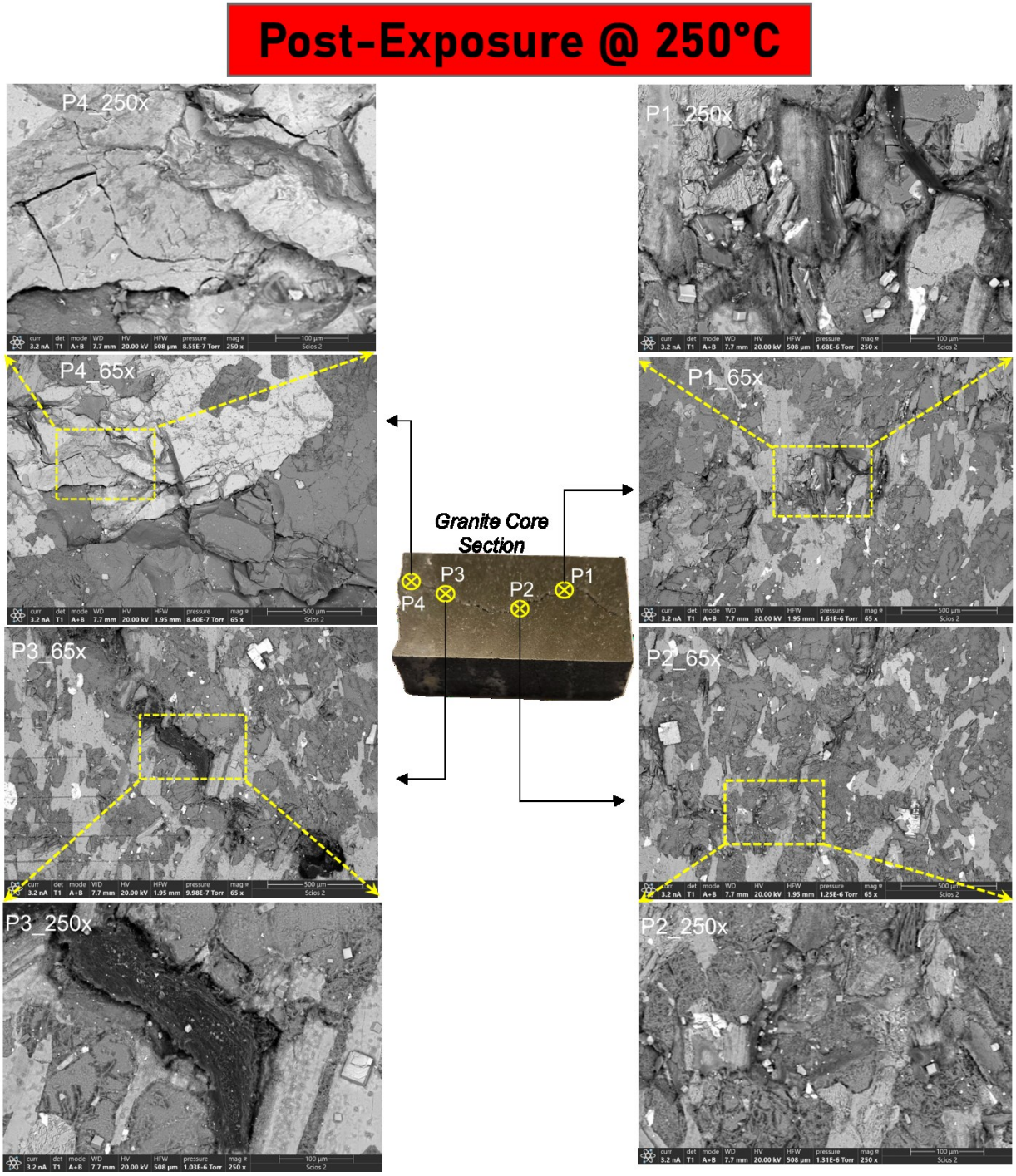

Figure 4. Post-exposure SEM–BSE microstructural evolution after hydrothermal treatment at 250 °C. SEM–BSE images of the same surface locations (P1–P4) following hydrothermal exposure at 250 °C illustrate microstructural and surface alterations relative to the pre-exposure state. Low-magnification images (65×) show changes in fracture connectivity, grain boundary definition, and contrast heterogeneity, while higher-magnification images (250×) reveal localized alteration features, secondary phase development, and fracture infill. Dashed yellow boxes denote the regions examined in detail. The central photograph indicates the correspondence between analyzed locations before and after exposure.

Point 3 shows the strongest localized response to hydrothermal exposure. Prior to testing, this location is dominated by a well-defined, elongated fracture with sharp walls and minimal evidence of chemical alteration. Post-exposure images reveal substantial modification concentrated within the fracture and its margins, including widening of the fracture trace, diffuse and embayed boundaries, and infill by dark, texturally complex material. These features indicate focused fluid penetration along the pre-existing fracture, leading to localized dissolution, secondary phase development, and weakening of the adjacent matrix.

In contrast, Point 4 exhibits a comparatively restrained alteration response. Pre-exposure images show a massive, blocky grain framework with limited fracture density. Following hydrothermal treatment, the overall fabric remains intact, with alteration largely restricted to subtle changes along existing microfractures and grain boundaries. Grain interiors retain homogeneous BSE contrast, and accessory phases remain sharply defined, indicating limited chemical penetration into intact crystalline domains.

Overall, the SEM–BSE observations demonstrate that hydrothermal alteration at 250 °C is strongly controlled by initial microstructural characteristics, particularly fracture density and connectivity. Within fracture-associated regions, microstructural modification is spatially heterogeneous. Domains characterized by higher local fluid access such as fracture intersections, widened apertures, and grain boundary–rich segments, exhibit more pronounced alteration, whereas adjacent fracture-proximal but comparatively less accessible domains show limited modification. These results highlight the critical role of inherited microstructure in governing the spatial distribution and intensity of hydrothermal surface alteration.

3.3. EDS Mapping and Elemental Redistribution

Energy-dispersive X-ray spectroscopy (EDS) mapping was used to evaluate mineralogical redistribution and element-scale modification induced by hydrothermal exposure at 250 °C. Unlike point-based analyses, EDS phase maps provide spatially continuous information on the distribution of primary minerals, secondary alteration products, and fracture-related domains, enabling assessment of how fluid–rock interaction modifies mineral assemblages at the grain and sub-grain scale. Pre- and post-exposure EDS maps from identical surface locations (P1–P4; Figures 5 and 6) were compared to isolate hydrothermally driven changes from inherited mineralogical heterogeneity.

Pre-exposure EDS maps show a coherent igneous mineral framework dominated by plagioclase, biotite, hornblende, quartz, titanite, and accessory Fe–Ti oxides. Primary mineral domains are compositionally discrete, with sharp grain boundaries and limited mixed or diffuse regions. Fracture- and void-related domains are clearly defined but largely unfilled, indicating minimal pre-existing secondary mineralization prior to hydrothermal treatment.

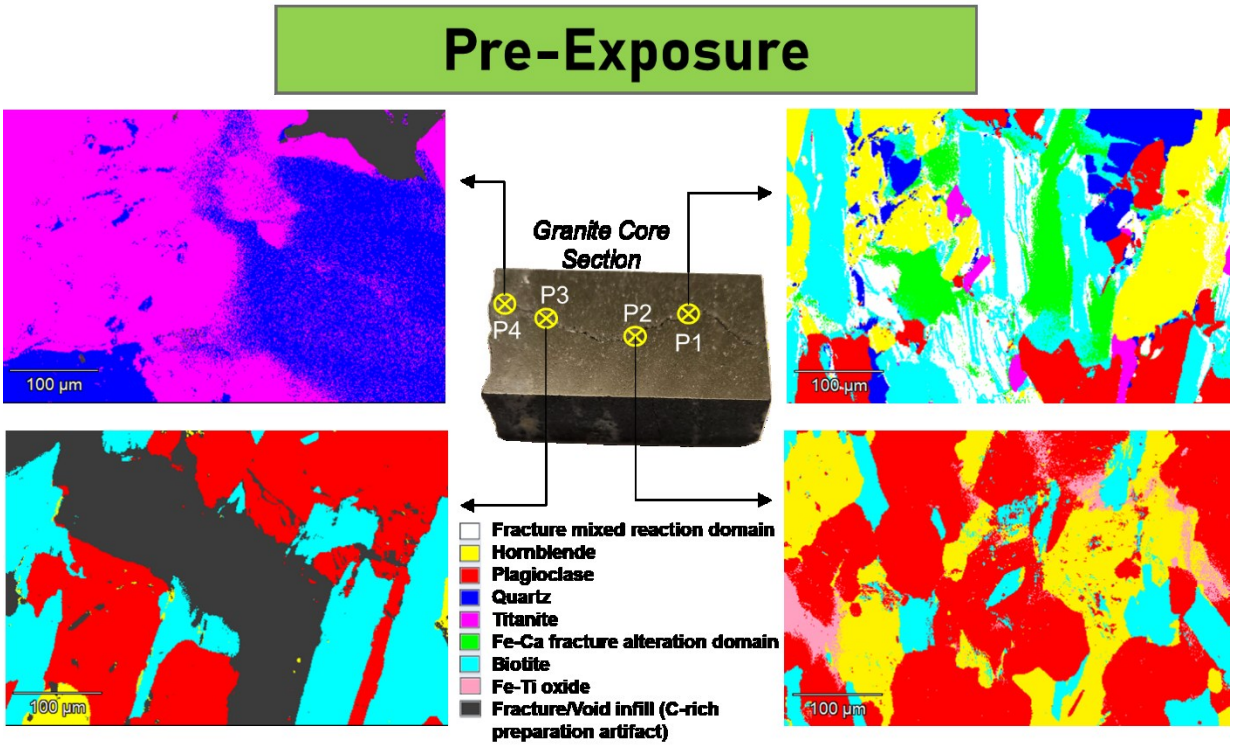

Figure 5. Pre-exposure EDS phase maps of the granite core surface showing the spatial distribution of primary mineral phases at four analyzed locations (P1–P4). The central photograph indicates the relative positions of the mapped areas on the core. Individual maps illustrate the heterogeneous but compositionally coherent pre-exposure mineral framework, dominated by plagioclase, biotite, hornblende, quartz, titanite, and accessory Fe–Ti oxides, with fracture and void domains clearly delineated. These maps establish the baseline mineralogical architecture prior to hydrothermal treatment at 250 °C.

Post-exposure EDS maps reveal systematic and spatially heterogeneous elemental redistribution across all four locations. The most pervasive change is the development of secondary aluminosilicate alteration, which partially replaces primary plagioclase and ferromagnesian silicates and forms compositionally diffuse domains that cross-cut original grain boundaries. These altered regions are

preferentially concentrated along grain boundaries, cleavage planes, and fracture-connected pathways, indicating dissolution–reprecipitation processes controlled by microstructural accessibility.

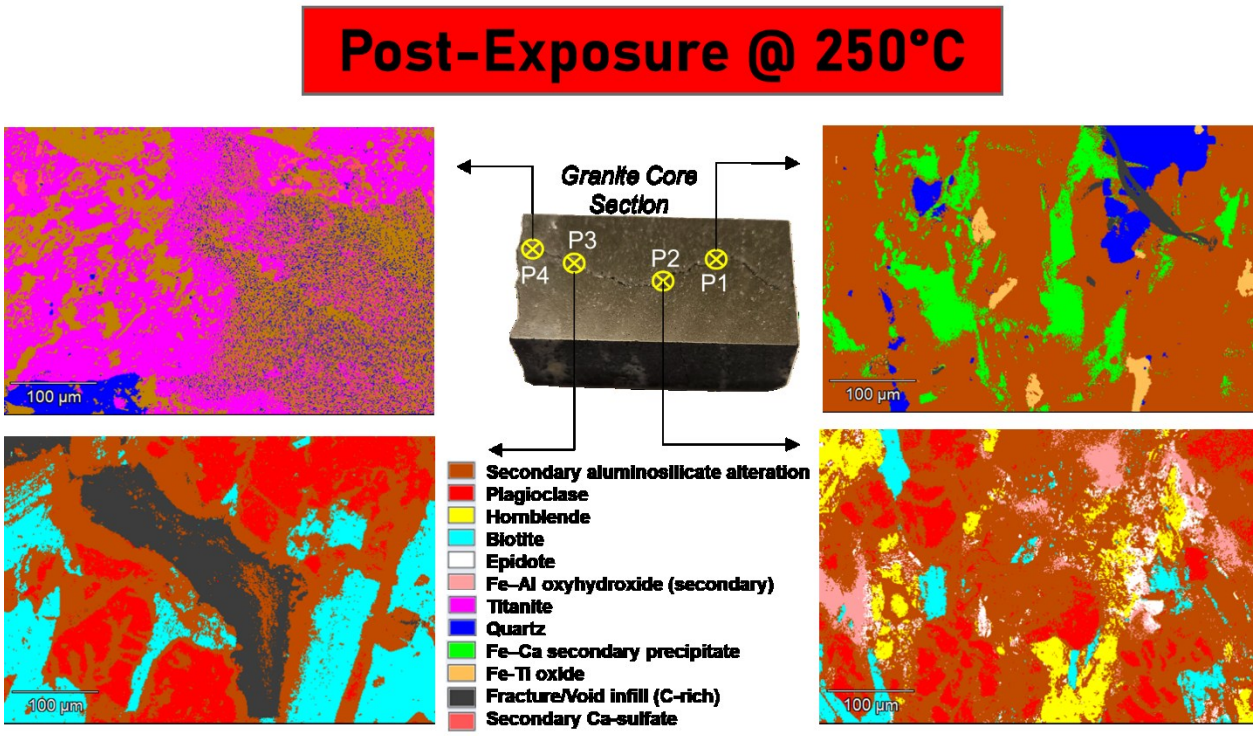

Figure 6. Post-exposure EDS phase maps of the granite core surface after hydrothermal treatment at 250 °C, showing mineralogical redistribution at the same four locations (P1–P4) identified in Figure X. The central photograph marks the mapped positions on the core. Compared with the pre-exposure state, the maps reveal the development of secondary alteration products, including secondary aluminosilicates, Fe-bearing phases, and localized Ca-sulfate precipitation, alongside attenuation and fragmentation of primary mineral domains. Alteration is spatially heterogeneous and preferentially concentrated along fractures, grain boundaries, and other fluid-accessible pathways.

At Points 1 and 2, alteration is relatively widespread, with secondary aluminosilicates and Fe-bearing phases overprinting large portions of the mapped areas. The appearance of Fe–Al oxyhydroxides, locally accompanied by epidote at Point 2, indicates mobilization of Fe, Al, and Ca from primary minerals and subsequent reprecipitation under hydrothermal conditions. Biotite- and hornblende-rich domains show the strongest modification, while quartz remains largely stable and retains coherent domains in all cases. At Point 3, elemental redistribution is strongly fracture-dominated. A pre-existing void/fracture acts as a focused fluid conduit, becoming partially to extensively infilled by secondary aluminosilicate material after exposure. Alteration is sharply localized to the fracture interior and adjacent margins, with limited penetration into the surrounding matrix, demonstrating the dominant role of inherited structural discontinuities in controlling reaction pathways. Point 4 exhibits the most mineralogically restrained response. The pre-exposure assemblage is dominated by titanite and quartz, which largely persist after exposure. However, post-exposure maps reveal localized development of secondary aluminosilicates and discrete secondary Ca-sulfate precipitation associated with fracture-adjacent regions. The occurrence of Ca-sulfate, absent in the pre-exposure state, indicates fluid-mediated mobilization of Ca and localized precipitation within chemically accessible domains rather than bulk transformation of titanite.

Across all analyzed locations, fracture and void domains classified as “fracture/void infill” correspond to carbon-rich residues introduced during sample preparation, primarily residual mounting wax and polishing media that infiltrated open fractures by capillary action during grinding and polishing. These domains are therefore treated as preparation artifacts and excluded from mineralogical interpretation. Excluding these regions, the EDS results demonstrate that hydrothermal alteration at 250 °C is highly heterogeneous and strongly controlled by the coupled effects of mineral reactivity and microstructural fluid access. Elemental redistribution is preferentially localized along fractures and other mechanically weak pathways rather than uniformly distributed throughout the rock matrix, consistent with SEM–BSE observations and reinforcing the role of fracture-controlled transport in governing hydrothermal alteration processes.

3.4. Elemental Redistribution in DI Water Induced by High-Temperature Fluid–Rock Interaction

Inductively coupled plasma–mass spectrometry (ICP-MS) analysis was used to quantify elemental concentrations in deionized (DI) water following high-temperature interaction with crystalline rock at 250 °C. The resulting elemental concentrations, summarized in Figure 7, provide direct evidence of solute acquisition by the fluid and enable assessment of element mobilization associated with hydrothermal fluid–rock interaction. As shown in Figure 7, the reacted DI water exhibits substantial enrichment in both major and trace elements relative to its initial composition. Alkali and alkaline earth elements display pronounced increases, particularly Si, K, Ca, Na, and Mg, indicating extensive dissolution of silicate and feldspathic phases. Silicon shows the largest absolute increase, consistent with dissolution of quartz and aluminosilicate minerals and in agreement with the widespread development of secondary aluminosilicate alteration observed in

SEM–EDS analyses. Elevated concentrations of Ca and K further reflect breakdown of plagioclase and Ca-bearing accessory phases, while increased Mg indicates interaction with ferromagnesian minerals such as biotite and hornblende.

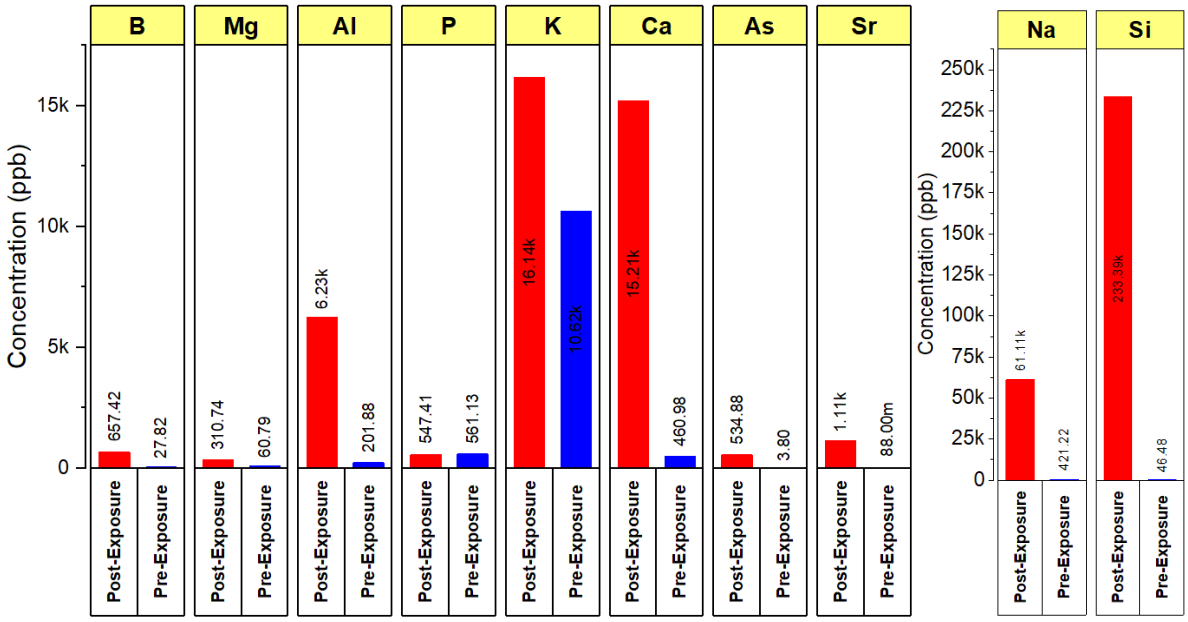

Figure 7. ICP-MS–derived elemental concentrations in deionized (DI) water before and after high-temperature interaction with crystalline rock at 250 °C. Bars compare unreacted DI water with reacted fluid, highlighting enrichment of major (e.g., Si, Na, K, Ca, Mg) and trace elements (e.g., Al, P, Sr, As, B) following hydrothermal exposure. Concentrations are reported in ppb. The observed solute enrichment reflects dissolution of silicate, feldspathic, and accessory mineral phases during fluid–rock interaction and is accompanied by a decrease in fluid pH from 7.2 to 5.45.

Trace elements including Al, P, Sr, As, and B are also measurably enriched in the reacted fluid (Figure 7). Aluminum mobilization, despite its typically low solubility, is consistent with the acidic conditions developed during the experiment and with the formation of secondary aluminosilicate and Fe–Al oxyhydroxide phases identified in post-exposure EDS maps. The presence of Sr suggests leaching from feldspar or accessory phases, whereas detectable as reflects trace-element release during mineral dissolution or desorption from mineral surfaces under hydrothermal conditions. The chemical evolution of the fluid is further reflected by a decrease in pH from 7.2 prior to exposure to 5.45 after hydrothermal interaction, consistent with proton-generating hydrolysis reactions during silicate dissolution. This acidification would enhance dissolution kinetics of feldspars and ferromagnesian minerals, promote continued element release and reinforcing the coupled chemical–mineralogical evolution observed in the solid phase.

Overall, the ICP-MS data presented in Figure 7 demonstrate that nominally DI water becomes chemically reactive under elevated-temperature conditions, acquiring a distinct elemental signature through interaction with crystalline rock. The combined enrichment of dissolved species and reduction in pH provides independent geochemical evidence for active mass transfer between fluid and rock during hydrothermal exposure at 250 °C.

3.5. Nano-Scale Mechanical Properties

Nanoindentation experiments were performed using a Nanovea P-Nano/Micro mechanical tester (Nanovea Inc., CA, USA) equipped with a Berkovich three-sided diamond indenter (tip ID 0104). The diamond indenter has a nominal elastic modulus of 1140 GPa and a Poisson's ratio of 0.07. All tests were conducted under load-controlled conditions using a maximum load of 10 mN, with loading and unloading rates of 20 mN min^{-1}. An approach speed of 10 µm min^{-1} and a contact load of 0.5 mN were employed to ensure stable surface engagement prior to loading. Figure 8 depicts Schematic and experimental overview of the nanoindentation methodology.

A creep (hold) segment of 10 s at peak load was included in each indentation cycle to reduce the influence of time-dependent deformation and thermal drift on the extracted elastic modulus and hardness values. This hold period is particularly important for crystalline rocks subjected to hydrothermal alteration, where secondary aluminosilicate phases and micro-porosity may introduce viscoelastic or creep-like responses at the indentation scale.

Nanoindentation mapping was carried out in region 3, selected as the primary area of interest within the scanned surface. This region was chosen because it represents a mechanically and mineralogically representative domain away from major open fractures, while still capturing the cumulative effects of hydrothermal exposure on the crystalline matrix. Focusing on Region 3 minimizes the influence of extreme edge effects and void-controlled compliance that can dominate indentation responses near fully open fractures, allowing a more reliable assessment of matrix-scale mechanical degradation relevant to fracture wall behavior in EGS.

A structured indentation grid was implemented consisting of 46 indentations in the horizontal direction and 6 indentations in the vertical direction, yielding a total of 276 nominal indentation sites. The inter-indentation spacing was set to 42 µm laterally and 205 µm vertically, which is sufficient to prevent plastic zone interaction between adjacent indents at the applied load level while enabling spatial mapping

of mechanical heterogeneity across the region. This spacing strategy balances statistical coverage with mechanical independence, ensuring that each indentation probes an effectively undisturbed material volume.

All indentation locations were recorded in the instrument coordinate system (X–Y), enabling subsequent spatial correlation with microstructural and mineralogical observations. The resulting elastic modulus and hardness maps provide a quantitative basis for comparing pre- and post-hydrothermal exposure mechanical behavior within the same region and at the same length scale. Mechanical properties, including hardness (H) and elastic modulus (E), were determined using the Oliver and Pharr method (Oliver & Pharr, 1992).

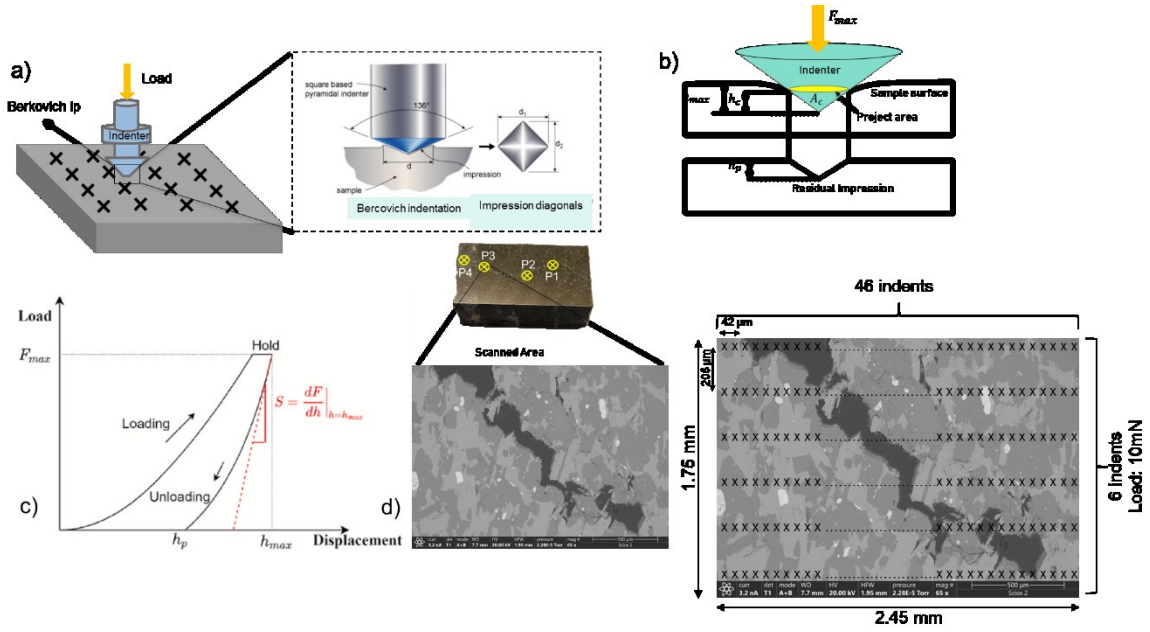

Figure 8. Schematic and experimental overview of the nanoindentation methodology. The figure illustrates (a) the nanoindentation mapping concept applied to the polished sample surface, (b) the geometry of the diamond indenter and resulting indentation imprint, (c) a representative load–displacement curve highlighting the loading, hold, and unloading segments used to extract mechanical properties, and (d–f) the selection of the region of interest and the corresponding microstructural context used to guide indentation placement and spatial analysis.

3.5.1. Interpretation of Nanoindentation Results and Implications of Hydrothermal Alteration

The multi-panel statistical comparison of nanoindentation results (Figure 9) demonstrates a pronounced and systematic reduction in both hardness and elastic modulus following hydrothermal exposure at 250 °C. Probability density histograms plotted on a logarithmic scale (Figure 9a,b) show a clear leftward shift of the post-exposure distributions relative to the pre-exposure state, spanning nearly one order of magnitude for hardness and more than half an order of magnitude for elastic modulus. This shift indicates pervasive mechanical weakening rather than localized or sporadic degradation.

This interpretation is reinforced by the cumulative distribution functions (Figure 9c,d), which show a consistent displacement of the post-exposure curves toward lower values across the full percentile range. The uniform separation between pre- and post-exposure CDFs indicates that softening affects the majority of indentation sites. In addition, the increased slope of the post-exposure CDFs at low values reflects a larger population of mechanically compliant responses, consistent with alteration-induced damage and the development of weaker secondary phases.

Boxplot comparisons (Figure 9e,f) further highlight the mechanical evolution induced by hydrothermal exposure. Median hardness and modulus values decrease markedly after exposure, while the interquartile ranges broaden, particularly for hardness. This increased dispersion reflects enhanced mechanical heterogeneity, suggesting uneven alteration of the crystalline matrix. The persistence of limited higher-value outliers implies that remnants of less-altered primary minerals remain locally intact, even though the dominant mechanical response is governed by weaker domains. Spatially resolved hardness and modulus maps (Figure 10) provide complementary insight into the nature of this mechanical degradation. Prior to exposure (Figure 10a,c), the maps exhibit strong spatial heterogeneity, with discrete high-stiffness and high-hardness domains associated with intact crystalline phases within the granite matrix.

After hydrothermal exposure (Figure 10b,d), these contrasts are largely suppressed, and the maps are dominated by uniformly low mechanical values, with only isolated patches retaining higher stiffness or hardness. This transition indicates that hydrothermal alteration not only reduces average mechanical properties but also diminishes mechanical contrast between mineralogical domains. The spatial correspondence between pre- and post-exposure maps confirms that the observed changes are not artifacts of indentation location or mapping geometry but rather reflect a genuine transformation of the near-surface mechanical framework within the same region.

The near-ubiquitous reduction in elastic modules implies increased local compliance of the fracture-adjacent matrix, while the concurrent reduction in hardness indicates a greater susceptibility to inelastic deformation and grain-scale yielding. These mechanical trends are consistent with the documented mineralogical evolution from a primary assemblage dominated by plagioclase, biotite, and hornblende

toward secondary aluminosilicate alteration products following hydrothermal exposure. Such alteration processes are known to reduce phase-scale stiffness and strength and to introduce microstructural damage, porosity, and fine-grained alteration textures, all of which contribute to lower indentation-derived hardness and modulus. The combined statistical and spatial results therefore support an interpretation in which mechanically weak alteration domains increasingly control the nano-scale response of the rock matrix.

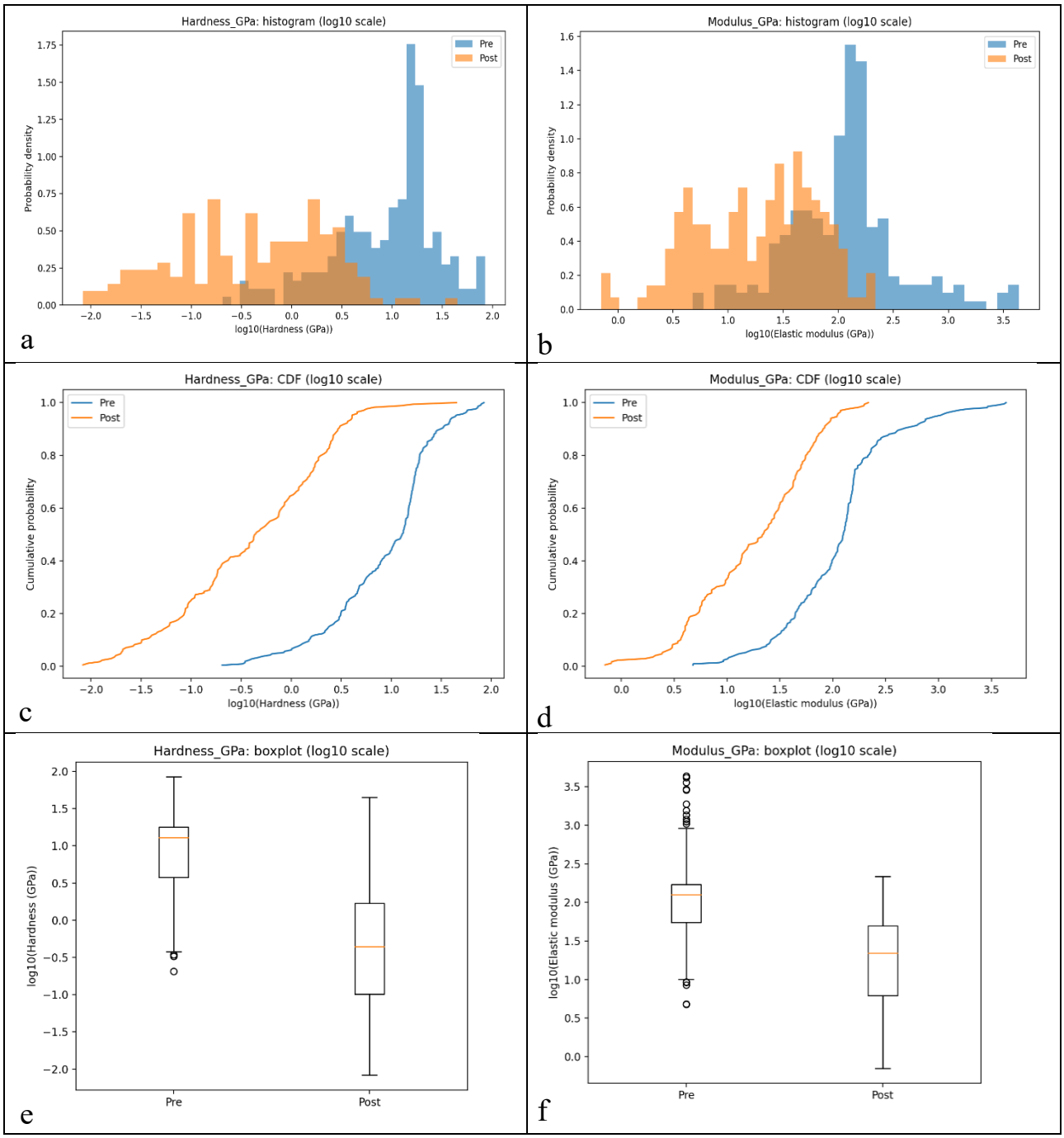

Figure 9. Statistical comparison of nanoindentation-derived mechanical properties before and after hydrothermal exposure at 250 °C. (a,b) Probability density histograms of hardness and elastic modulus plotted on a logarithmic scale, showing a systematic leftward shift of the post-exposure distributions toward lower values. (c,d) Cumulative distribution functions (CDFs) highlighting a consistent reduction in hardness and modulus across the full percentile range after exposure. (e,f) Box-and-whisker plots (log scale) illustrating the decrease in median values and increased variability following hydrothermal alteration. All results are derived from indentations performed within the same mapped region.

From an Enhanced Geothermal Systems perspective, this alteration-driven reduction in stiffness and hardness has direct implications for fracture mechanics and long-term reservoir performance. Increased fracture-wall compliance promotes greater fracture closure under effective stress, while reduced contact stiffness increases the likelihood of proppant embedment where proppants interact with a softened

fracture surface. Both effects act to reduce effective fracture aperture and fracture conductivity. The spatially widespread nature of the observed weakening suggests that these effects are governed by region-scale alteration of the rock matrix rather than localized edge or surface artifacts, underscoring the importance of hydrothermal alteration in controlling the mechanical evolution of crystalline reservoirs.

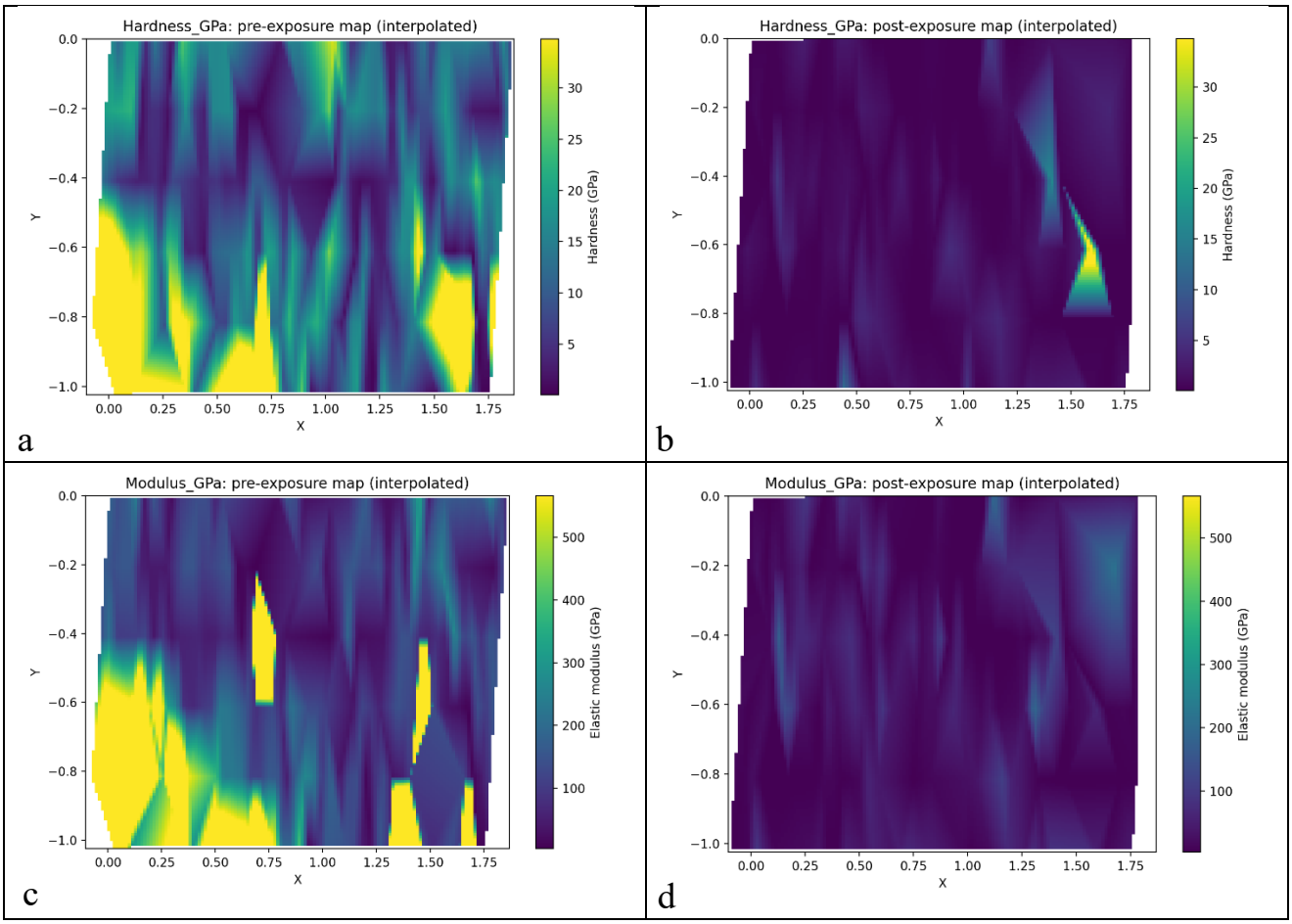

Figure 10. Spatial distribution of nanoindentation-derived mechanical properties before and after hydrothermal exposure at 250 °C. (a,b) Interpolated hardness maps for the pre- and post-exposure states, respectively. (c,d) Interpolated elastic modulus maps for the pre- and post-exposure states, respectively. Pre-exposure maps exhibit pronounced spatial heterogeneity associated with intact crystalline phases, whereas post-exposure maps are dominated by uniformly lower values, indicating widespread mechanical weakening of the rock matrix. Identical color scales are used for pre- and post-exposure maps to facilitate direct comparison.

The observed fracture-scale mineralogical and mechanical heterogeneity has direct implications for proppant design strategies in the Utah FORGE reservoir. SEM–BSE and EDS results demonstrate that hydrothermal interaction preferentially modifies fracture surfaces through the formation of heterogeneous aluminosilicate alteration coatings, Fe–Al–rich reaction layers, and localized Ca–F–bearing precipitates. These secondary phases locally reduce surface hardness and elastic modulus, as confirmed by nanoindentation, and introduce spatially variable mechanical compliance along fracture walls. Such heterogeneity implies that proppant–fracture contact conditions are non-uniform and evolve during thermal and chemical exposure. Consequently, proppants deployed in the FORGE reservoir must be mechanically robust against uneven load transfer, chemically stable in the presence of reactive fracture coatings, and tolerant of evolving surface roughness and local compliance. The results support the use of high-strength, chemically inert proppants with minimized surface reactivity, as well as the potential benefit of surface-modified or coated proppants designed to reduce adhesion to alteration products and mitigate embedment into softened fracture surfaces.

CONCLUSION

This study demonstrates that hydrothermal exposure at 250 °C induces tightly coupled microstructural, mineralogical, geochemical, and mechanical transformations in crystalline granite that are strongly governed by inherited microstructure. SEM–BSE observations show that alteration is spatially heterogeneous and preferentially localized along pre-existing fractures, grain boundaries, and other fluid-accessible pathways, while intact, low-permeability domains remain comparatively preserved. EDS phase mapping confirms that these microstructural pathways act as primary conduits for dissolution–reprecipitation reactions, leading to the development of secondary aluminosilicate and Fe-bearing phases, localized Ca-sulfate precipitation, and attenuation of primary feldspathic and ferromagnesian minerals. Complementary ICP-MS analysis of reacted DI water provides independent geochemical evidence for active mass transfer

during hydrothermal interaction, marked by substantial enrichment of major and trace elements and a pronounced decrease in pH. The chemical evolution of the fluid is consistent with silicate dissolution and supports the observed solid-phase alteration patterns. Nanoindentation results further reveal that these mineralogical and microstructural changes translate directly into mechanical degradation at the nano-scale, expressed as a systematic reduction in elastic modulus and hardness, increased mechanical heterogeneity, and suppression of high-stiffness domains following exposure.

Taken together, the results indicate that hydrothermal alteration progressively shifts the mechanical response of the granite from a heterogeneous, phase-controlled framework toward a more uniformly compliant matrix dominated by weak secondary alteration products. From an Enhanced Geothermal Systems perspective, this alteration-driven softening has important implications for fracture stability, fracture-wall compliance, and proppant–rock interactions, suggesting an increased propensity for fracture closure and proppant embedment under reservoir conditions. More broadly, the findings highlight the necessity of accounting for microstructure-controlled hydrothermal alteration when evaluating the long-term mechanical evolution and performance of crystalline geothermal reservoirs.

ACKNOWLEDGMENTS

This research was supported by the U.S. Department of Energy's Utah FORGE program under Contract UEI Number NNYDFK5FTSX9, Award Number 9-3706. The authors gratefully acknowledge the Utah FORGE team for providing wellbore core samples and extend special thanks for their generous feedback and support. The author gratefully acknowledges Dr. Mileva Radonjic for her foundational role in initiating and conceptualizing this project, for her guidance in defining the research direction, and for serving as the Principal Investigator who secured the funding that made this work possible. The majority of the experimental work was conducted in the Hydraulic Barrier and Geomimicry Laboratory at Oklahoma State University, with appreciation to Mr. Loic Bethel Dje for his valuable assistance. Portions of this study were performed in the OSU Microscopy Laboratory, supported by NSF MRI and DOE NETL equipment funding, special thanks are extended to Mr. Brent Johnson and Ms. Lisa Whitworth for their technical assistance. Additionally, we extend our gratitude to Dr. Puckette for granting access to geology laboratory for sample preparation.

REFERENCES

Allard, T., Ildefonse, P., VILLAR, L. P. Del, Sorieul, S., Pelayo, M., Boizot, B., Balan, E., & Calas, G. (2003). Radiation-induced defects in dickites from the EI Berrocal granitic system (Spain) relation with past occurrence of natural radioelements. *European Journal of Mineralogy*, *15*(4), 629–640.

Ayling, B., Rose, P., Petty, S., Zemach, E., & Drakos, P. (2012). QEMSCAN (Quantitative evaluation of minerals by scanning electron microscopy): capability and application to fracture characterization in geothermal systems. *Proc, Thirty-Seventh Workshop on Geotherm Reserv Eng. Stanford, California: Stanford University*.

Azim, M. R., Amin, M. S., & Shoeb, M. A. (2010). Prospect of enhanced geothermal system in baseload power generation. *2010 IEEE International Conference on Advanced Management Science (ICAMS 2010)*, *3*, 176–180.

Bächler, D., & Kohl, T. (2005). Coupled thermal–hydraulic–chemical modelling of enhanced geothermal systems. *Geophysical Journal International*, *161*(2), 533–548.

Callahan, O. A., Eichhubl, P., Olson, J. E., & Davatzes, N. C. (2019). Fracture mechanical properties of damaged and hydrothermally altered rocks, Dixie Valley-Stillwater Fault Zone, Nevada, USA. *Journal of Geophysical Research: Solid Earth*, *124*(4), 4069–4090.

Dobson, P. F., Kneafsey, T. J., Nakagawa, S., Sonnenthal, E. L., Voltolini, M., Smith, J. T., & Borglin, S. E. (2021a). Fracture sustainability in Enhanced Geothermal Systems: Experimental and modeling constraints. *Journal of Energy Resources Technology*, *143*(10), 100901.

Dobson, P. F., Kneafsey, T. J., Nakagawa, S., Sonnenthal, E. L., Voltolini, M., Smith, J. T., & Borglin, S. E. (2021b). Fracture sustainability in Enhanced Geothermal Systems: Experimental and modeling constraints. *Journal of Energy Resources Technology*, *143*(10), 100901.

Duan, X.-Y., Huang, D., Lei, W.-X., Chen, S.-C., Huang, Z.-Q., & Zhu, C.-Y. (2023). Investigation of Heat Extraction in an Enhanced Geothermal System Embedded with Fracture Networks Using the Thermal–Hydraulic–Mechanical Coupling Model. *Energies*, *16*(9), 3758.

Ettehadi, A., Mutume, B., & Radonjic, M. (2026). Mineral-mechanical heterogeneity of natural fractures in crystalline rocks: A case study from Utah FORGE. *Geothermics*, *134*, 103529.

Ettehadi, A., Mutume, B., Radonjic, M., Noori, H., & Dong, W. (2025). Cracking the Granite Code at Utah FORGE EGS: Insights into Salt Mobilization, Acidification, and Fluid-Induced Geochemical Alteration. *2025 Geothermal Rising Conference, Vol 49*, 1451–1475.

Forbes, B., Moore, J. N., Finnila, A., Podgorney, R., Nadimi, S., & McLennan, J. D. (2019). Natural fracture characterization at the Utah FORGE EGS test site—discrete natural fracture network, stress field, and critical stress analysis. *Geothermal Characteristics of the Roosevelt Hot Springs System and Adjacent FORGE EGS Site, Milford, Utah. Utah Geological Survey Miscellaneous Publication*, *169*.

Frash, L. P., Iyare, U. C., KC, B., Meng, M., Smith, M., & Kroll, K. (2024). High Temperature Triaxial Direct-Shear Testing for FORGE and Field Scale Implications. *ARMA US Rock Mechanics/Geomechanics Symposium*, D042S059R005.

Harpers, N., Forbes Inskip, N., Allen, M. J., Buckman, J., Faulkner, D. R., Claes, H., Shail, R., den Hartog, S., & Busch, A. (2024). Effects of chemical alteration on frictional properties in a deep, granitic, geothermal system in Cornwall: Direct shear experiments at near in situ conditions. *Journal of Geophysical Research: Solid Earth*, *129*(10), e2024JB028861.

Hueckel, T., Tao, F., Cassiani, G., & Pellegrino, A. (2001). Chemical softening and hardening of geomaterials in situ. *Computer Methods and Advances on Geomechanics*, *1*, 743–748.

Jeanloz, R., & Stone, H. A. (2014). JASON review of enhanced geothermal systems. *Proceedings, Thirty-Ninth Workshop on Geothermal Reservoir Engineering Stanford University, Stanford, California*.

Jones, T. A., & Detwiler, R. L. (2016). Fracture sealing by mineral precipitation: The role of small-scale mineral heterogeneity. *Geophysical Research Letters*, *43*(14), 7564–7571.

Kumawat, P. K., Deo, M., McLenann, J., & Panja, P. (2025). Effect of Fracture Connectivity between Production and Injection Wells in Enhanced Geothermal Systems (EGS). *ARMA US Rock Mechanics/Geomechanics Symposium*, D021S004R001.

Ledésert, B., Hebert, R., Genter, A., Bartier, D., Clauer, N., & Grall, C. (2010). Fractures, hydrothermal alterations and permeability in the Soultz Enhanced Geothermal System. *Comptes Rendus. Géoscience*, *342*(7–8), 607–615.

Mattson, E. D., Neupane, G., Plummer, M., Jones, C., & Moore, J. (2016). *Long-term sustainability of fracture conductivity in geothermal systems using proppants*. Idaho National Lab.(INL), Idaho Falls, ID (United States).

Meller, C., Bremer, J., Baur, S., Bergfeldt, T., Blum, P., Canic, T., Eiche, E., Gaucher, E., Hagenmeyer, V., & Heberling, F. (2017). Integrated research as key to the development of a sustainable geothermal energy technology. *Energy Technology*, *5*(7), 965–1006.

Miller, J., Allis, R., & Hardwick, C. (2019). Interpretation of seismic reflection surveys near the FORGE enhanced geothermal systems site, Utah. *Geothermal Characteristics of the Roosevelt Hot Springs System and Adjacent FORGE EGS Site; Allis, R., Moore, JN, Eds*, 13.

Murphy, H. D., Tester, J. W., Grigsby, C. O., & Potter, R. M. (1981). Energy extraction from fractured geothermal reservoirs in low-permeability crystalline rock. *Journal of Geophysical Research: Solid Earth*, *86*(B8), 7145–7158.

Mutume, B., Ettehadi, A., Dhanapala, B. D., Palisch, T., Dong, W., & Radonjic, M. (2025). Geochemical Reactivity and Alteration Mechanisms of Proppant Materials in Enhanced Geothermal Systems. *2025 Geothermal Rising Conference, Vol 49*, 1172–1181.

Mutume, B., Ettehadi, A., Dhanapala, B. D., Palisch, T., & Radonjic, M. (2025). Multiscale Characterization of Thermo-Hydro-Chemical Interactions Between Proppants and Fluids in Low-Temperature EGS Conditions. *Energies*, *18*(15), 3974.

Mutume, B., Ettehadi, A., Radonjic, M., Dhanapala, B. D., & Palisch, T. (2025). Geochemical Interactions of Proppants with Utah FORGE Fluids: Insights from Moderate-Temperature Experiments. *ARMA US Rock Mechanics/Geomechanics Symposium*, D031S036R005.

Oliver, W. C., & Pharr, G. M. (1992). An improved technique for determining hardness and elastic modulus using load and displacement sensing indentation experiments. *Journal of Materials Research*, *7*(6), 1564–1583.

Pritchett, J. W. (2008). *Evaluating Permeability Enchancement Using Electrical Techniques*. SAIC.

Sanyal, S. K. (2009). Optimization of the economics of electric power from enhanced geothermal systems. *Proceedings, Thirty-Fourth Workshop on Geothermal Reservoir Engineering, Stanford University, Stanford, California*.

Schuster, V., Rybacki, E., Schleicher, A. M., Koirala, R., & Göbel, T. H. W. (2025). The effect of hydrothermal alteration and microcracks on hydraulic properties and poroelastic deformation: A case study of the Blue Mountain geothermal field. *Journal of Geophysical Research: Solid Earth*, *130*(4), e2024JB030541.

Shan, K., Zou, Q., Li, C., & Yu, Z. (2024). Advancements and Future Prospects in the Hydraulic Fracturing of Geothermal Reservoirs. *Energies*, *17*(23), 6082.

Tao, J., Wu, Y., Elsworth, D., Li, P., & Hao, Y. (2019). Coupled thermo-hydro-mechanical-chemical modeling of permeability evolution in a Co2-circulated geothermal reservoir. *Geofluids*, *2019*(1), 5210730.

Tester, J. W., Anderson, B. J., Batchelor, A. S., Blackwell, D. D., DiPippo, R., Drake, E. M., Garnish, J., Livesay, B., Moore, M. C., & Nichols, K. (2007). Impact of enhanced geothermal systems on US energy supply in the twenty-first century. *Philosophical Transactions of the Royal Society A: Mathematical, Physical and Engineering Sciences*, *365*(1853), 1057–1094.

Tyurin, A. I., Victorov, S. D., Kochanov, A. N., Shuklinov, A. V, & Pirozhkova, T. S. (2016). Methods of micro-and nanoindentation for characterization of local physical and mechanical properties of multiphase materials. *AIP Conference Proceedings*, *1783*(1), 020227.

Willis-Richards, J., Watanabe, K., & Takahashi, H. (1996). Progress toward a stochastic rock mechanics model of engineered geothermal systems. *Journal of Geophysical Research: Solid Earth*, *101*(B8), 17481–17496.

Wu, Z., Edelman, E., Ritterbush, K., & McPherson, B. (2024). Quantifying the Uncertainties of Macro-and Micro-Mechanical Measurements on Sequestration Reservoir Formations. *ARMA US Rock Mechanics/Geomechanics Symposium*, D041S044R003.

Ye, Z., Ghassemi, A., & Kneafsey, T. (2020). Deformation, failure and permeability evolution of sealed fractures/foliations in EGS collab poorman schist. *ARMA US Rock Mechanics/Geomechanics Symposium*, ARMA-2020.

Zhang, Y., Pan, L., Dobson, P., Oglesby, K., & Finsterle, S. (2012). Microholes for improved heat extraction from EGS reservoirs: numerical evaluation. *Proceedings of the Thirty-Seventh Workshop on Geothermal Reservoir Engineering, Stanford University, Stanford, CA*, 1–6.